

Electrocatalytic Degradation of Methyl Orange using Nano- Fe_3O_4 Supported on Conductive Carbon Black as Particle Electrode

Miaomiao Sun, Yuzeng Zhao*, Honghua Ge*

Shanghai Engineering Research Center of Energy-Saving in Heat Exchange Systems, Shanghai Key Laboratory of Materials Protection and Advanced Materials in Electric Power, College of Environmental and Chemical Engineering, Shanghai University of Electric Power, Shanghai, 200090, China

*E-mail: zhaoyuzeng@shiep.edu.cn, gehonghua@shiep.edu.cn

Received: 29 April 2022 / Accepted: 7 June 2022 / Published: 4 July 2022

Using conductive carbon black (CCB) as a carrier, a heterogeneous catalyst with Fe_3O_4 as the active material ($\text{Fe}_3\text{O}_4/\text{CCB}$) was prepared by the impregnation method, and its performance in degrading of high-concentration methyl orange (MO) wastewater in the three-dimensional electro-Fenton system (3DEF) was explored. Characterization by TEM and XRD showed that Fe_3O_4 was uniformly loaded on CCB, and due to the synergistic effect of Fe_3O_4 and CCB in promoting degradation of pollutants, the degradation rate of this catalyst was 2.14 times higher than that of Fe_3O_4 alone. Under the optimal conditions, the COD removal rate and MO decolorization rate reached the maximum, values of 75.02% and 93.75%, respectively. After 5 cycles, the MO degradation rate was still 83.83%, indicating that the prepared particle electrode has good reusability. In addition, a reasonable catalytic mechanism of the 3DEF system for MO mineralization was proposed, confirming that the hydroxyl radicals were particularly important in the oxidation.

Keywords: COD removal rate; Decolorization rate of MO; Electrocatalytic oxidation; $\text{Fe}_3\text{O}_4/\text{CCB}$ particle electrode

1. INTRODUCTION

Water pollution attributed to organic emissions, especially the textile industry, has become a serious environmental concern [1]. Azo dyes with one or more $-\text{N}=\text{N}-$ groups are the foremost pollutants in textile wastewater. Their structures are complex, and they are usually stable in the water environment. They harm human health and aquatic organisms [2]. A variety of methods such as adsorption [3], flocculation [4], membrane separation [5], photo-Fenton process [6], ozone oxidation [7], and

electrocatalytic oxidation [8], have been used to treat dye wastewater. Comparatively, electrocatalytic oxidation as an advanced oxidation process (AOP), possesses many advantages, incorporating high efficiency, low energy consumption, and convenient operation [9-11], and is generally considered to be the most promising method.

AOPs, processes based on producing hydroxyl radical strong oxidants, have been broadly used to remove organic matter [12]. Among them, the three-dimensional (3D) electro-Fenton process is an effective method to degrade refractory organic compounds [13,14], including dyes [15], oil refining wastewater [16], phenolic compounds [17], pharmaceutical compounds [18], etc. In the 3D electro-Fenton system, the catalyst particles are charged to form tiny electrodes, thus shortening the mass transfer distance and greatly improving the current utilization rate. However, the problems of particle agglomeration, low recyclability, and high dependence on the main electrode still exist, hindering its practical application [19]. To overcome these shortcomings, exploring a novel type of catalyst particle with high catalytic activity is imperative.

Metal oxide nanomaterials have been widely studied by scholars for their advantages, such as economy, environmental protection, non-toxicity, and energy-saving [20]. Magnetite nanoparticles are often used as catalysts in 3D electro-Fenton systems due to their high catalytic activity and good magnetic separation performance, but magnetite is prone to agglomeration, weakens pollutant treatment effect [21]. This study improved upon this basis. In this research, a catalyst containing Fe_3O_4 was circulated in the reactor, and the dissolved Fe^{2+} participated in the Fenton reaction. The production of Fe^{2+} was mainly achieved through anodization and the redox reaction between iron and hydrogen ions. The oxygen molecules on the cathode surface generated H_2O_2 through a reduction reaction. The generated H_2O_2 rapidly reacted with Fe^{2+} in the solution to form $\cdot\text{OH}$ radicals, which can oxidize and degrade organic matter non-selectively. Since the reduction potential of Fe^{3+} is higher than that initial of O_2 , in the process of reducing O_2 , Fe^{3+} can be reduced and regenerated into Fe^{2+} [22].

Conductive carbon black (CCB) has a large specific surface area and excellent conductivity. Its rough surface is conducive to the adhesion of nanoparticles, which is the optimal choice of carrier. Because the unique hexagonal network layer structure of CCB can provide channels for O_2 diffusion, increase the active sites of the cathode, and CCB is easy to obtain at a low price [23]. Therefore, choosing CCB as the carrier of iron-based catalysts can not only improve the catalytic activity of magnetite nanoparticles, but also reduce the loss and agglomeration of catalysts, which is of great benefit to industrialization.

Iron carbon composite nanoparticles are often used as catalysts for wastewater treatment [24]. Fe_3O_4 has the advantages of simple preparation, low cost and high chemical stability. However, its low specific surface area leads to fewer active sites, and the low current efficiency restricts its practical application [25], while CCB alone has poor performance. CCB is stable owing to its porous structure. Combining the two to prepare $\text{Fe}_3\text{O}_4/\text{CCB}$ nanoparticle electrodes may provide the advantages of both. Placing the nanoparticle electrodes in an electrochemical reaction system can promote oxygen reduction and electro-Fenton reaction. Sufficient hydroxyl radicals can be produced without additional hydrogen peroxide to oxidize and degrade wastewater, which is an advantage different from traditional oxidation processes [26]. Methyl orange (MO) is extensive used and difficult to degrade, so it is often chosen as the target dye pollutant to test the performance of catalysts.

Herein, we prepared magnetic iron oxide-supported CCB ($\text{Fe}_3\text{O}_4/\text{CCB}$) catalyst nanoparticles using a simple impregnation method as an electrocatalyst to degrade simulated MO wastewater. Electrochemical impedance spectroscopy (EIS) and linear sweep voltammetry (LSV) were used to analyze the electrochemical performance of the $\text{Fe}_3\text{O}_4/\text{CCB}$ catalyst. The impacts of the applied voltage, pH value, electrolyte concentration, catalyst dosage, simulated MO wastewater concentration and current density on chemical oxygen demand (COD) removal rate and decolorization rate of simulated MO wastewater were investigated. The catalytic oxidation mechanism was further analyzed by radical quenching experiments.

2. MATERIALS AND METHODS

2.1 Materials

$\text{FeCl}_3 \cdot 6\text{H}_2\text{O}$, $\text{FeSO}_4 \cdot 7\text{H}_2\text{O}$ and MO were purchased from China Titan Co., Ltd. CCB was obtained from Shanghai Chenqi Chemical Technology Co., Ltd. Tert-butyl alcohol (TBA, 99%) was bought from Shanghai Aladdin Biochemical Technology Co., Ltd. All of the chemicals were analytical grade, and used directly without further purification.

2.2 Preparation of $\text{Fe}_3\text{O}_4/\text{CCB}$ particle electrodes

Pretreatment of CCB: CCB was heated and refluxed in a 3:1 mixture dilute solution of H_2SO_4 and HNO_3 at 80 °C for 40 minutes. When the reflux was completed, CCB was rinsed with deionized water many times until it became neutral. Then, it was dried at 80 °C.

Synthesis of catalysts: In a three-necked flask, 0.15 mol/L $\text{FeCl}_3 \cdot 6\text{H}_2\text{O}$ and 0.1 mol/L $\text{FeSO}_4 \cdot 7\text{H}_2\text{O}$ were dissolved in 100 mL deionized water, and then 2.0 g CCB was added to the flask. Ammonia was slowly dripped into the reaction solution with magnetic stirring under nitrogen protection. The solution temperature was maintained at 40 °C, and the pH value of the solution was monitored in real time. Dropping of ammonia was stopped when the reaction solution gradually turned dark and the pH value of the solution reached 10. The obtained suspension was stirred and insulated for 30 minutes. The filtered raw product from the suspension was washed sequentially with ethanol and deionized water, and then dried at 80 °C for 12 h under vacuum. Finally, the raw product was calcined for 2 h at 400 °C in a nitrogen-protected tubular furnace, and the temperature was increased by 5 °C/min. The prepared $\text{Fe}_3\text{O}_4/\text{CCB}$ particle electrodes were stockpiled in a vacuum container.

2.3 Electrocatalytic degradation experiments

Electrocatalytic degradation experiments were carried out in a 500 mL beaker. Two graphite electrode plates of the same size (10×5×3 mm) served as the cathode and anode for the catalytic system, which were positioned 2 cm away from the bottom of the beaker. The two electrodes maintained a constant distance of 4 cm. Under a DC power supply, the synthesized $\text{Fe}_3\text{O}_4/\text{CCB}$ particle electrodes

form a 3D electrochemical system to degrade the simulated MO wastewater. All experiments were performed at room temperature. The experimental setup is shown in Figure 1.

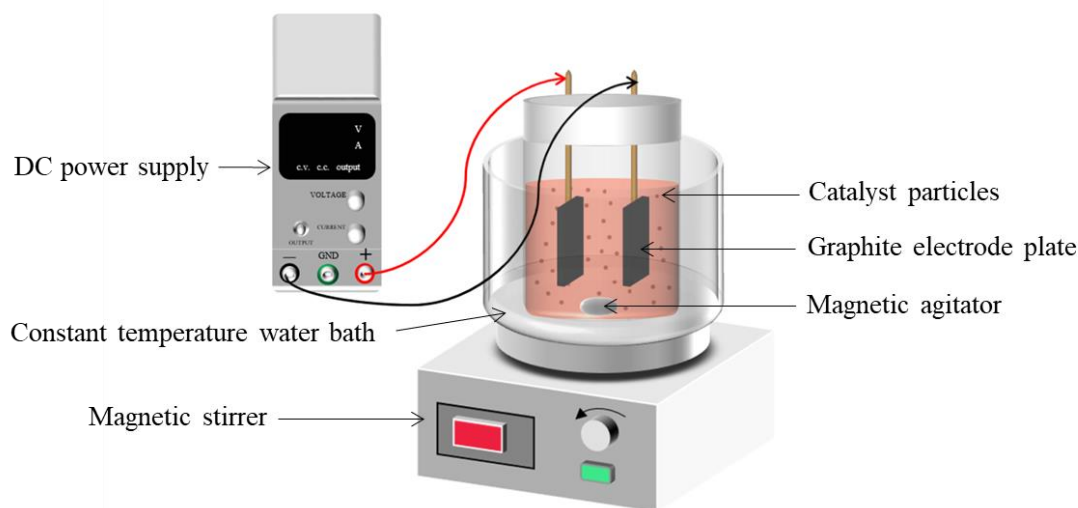


Figure 1. Response device diagram

2.4 Characterization of the Fe_3O_4/CCB catalyst

The Fe_3O_4/CCB catalyst was characterized through transmission electron microscopy (TEM, JEOL JEM 2100), and analyzed with X-ray diffraction (XRD, Bruker D8 Advance). The magnetic properties of the catalyst particles were determined using a vibrating sample magnetometer (VSM, LakeShore7404). The electrochemical performance of the Fe_3O_4/CCB particle electrodes was evaluated on an electrochemical workstation (CHI 660E, Chenhua Instruments). The three-electrode system consisted of a glassy carbon electrode (GCE) coated with the catalyst, a Pt sheet and a saturated calomel electrode (SCE). The manufacturing steps of the working electrode were as follows: 5 mg catalyst powder and Nafion (5 wt%, 15 μ L) were dispersed in 1 mL ethanol with ultrasonic stirring to obtain a slurry to be determined. Then, 10 μ L of the slurry was coated on the GCE. The oxidation-reduction performance of the Fe_3O_4/CCB particle electrodes was determined by LSV in a simulated MO wastewater solution with a 50 mV/s scan rate. EIS was performed in the frequency range of 100000 to 0.1 Hz.

2.5 Analytic procedure

The concentration of MO was determined by ultraviolet-visible spectroscopy. H_2O_2 concentration was determined using the titanium salt spectrophotometry method [27]. The $\cdot OH$ radical concentration in the system was measured by the fluorescence method, which mainly depended on the characteristic signal of 2-hydroxybenzoic acid produced by the reaction of $\cdot OH$ and terephthalic acid [28]. To further identify the intermediates and degradation pathway of MO, a UV-vis spectrophotometer

(Shimadzu, UV-2700) was applied to scan the MO solutions before and after degradation at 200~800 nm wavelength. The three-dimensional fluorescence method (RF-5301pc) showed the change of organic matter in the degradation process.

The COD removal rate and decolorization rate were used to evaluate the catalytic effect of the Fe₃O₄/CCB catalyst. During the reaction, 10 mL samples were taken every 15 min and filtered by 0.22 μm filter membrane for further testing. The calculation formula is below:

$$\text{Decolorization (\%)} = \frac{A_0 - A_t}{A_0} \times 100$$

Where A₀ and A_t represent the absorbance of MO at the initial and degradation time t, respectively.

The COD values were read out by a Lianhua water quality tester. Moreover, the calculation formula is below:

$$\text{COD removal (\%)} = \frac{\text{COD}_0 - \text{COD}_t}{\text{COD}_0} \times 100$$

Where COD₀ and COD_t are the COD of MO at the initial and degradation time t, respectively. All results were the average of three experiments.

3. RESULTS AND DISCUSSION

3.1 TEM, XRD and VSM analyses

The morphology of the CCB, Fe₃O₄ and Fe₃O₄/CCB particle electrodes was observed with TEM. Figure 2(a), shows that the surface of CCB is rough and uneven, which is conducive to loading of nanoparticles. Typical TEM micrographs of Fe₃O₄ (Figure 2(b)) clearly shows an obvious particle cluster phenomenon. The average size of the nanoparticles is also measured by counting more than 100 particles in different regions using TEM. Figure 2(c) shows the histogram of the average diameter distribution of the catalyst particles. The average size of the nanoparticles was 12.2 nm, which was very similar to the value obtained by XRD analysis. In contrast, the micrograph of Fe₃O₄/CCB showed a denser structure, as shown in Fig. 2(d). The results displayed that Fe₃O₄ was uniformly loaded on the surface of the CCB particles. Further elements of Fe₃O₄/CCB particle electrodes were identified by energy dispersive spectrometer (EDS) analysis, which confirmed the existence of Fe, C and O elements (Figure 2(e, f)). The proportions of Fe and O in the catalyst are 8.30% and 17.32%, respectively. (Explanation: The copper element was present because the test sample was swept out of a copper mesh).

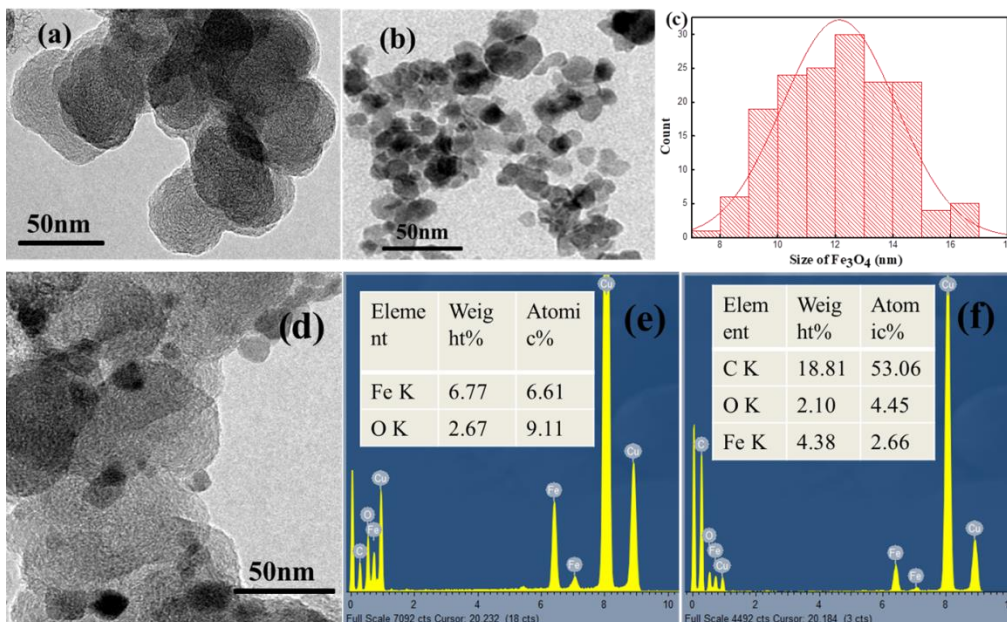


Figure 2. TEM pictures of (a) CCB; (b) Fe₃O₄; (c) particle size image of Fe₃O₄; (d) Fe₃O₄/CCB; (e)-(f) EDS spectras of Fe₃O₄ and Fe₃O₄/CCB.

The structure of the Fe₃O₄/CCB catalysts was indicated by XRD patterns (Figure 3). The CCB pattern exhibited a strong bulge peak near ($2\theta = 25^\circ$) and a weak (100) diffraction peak near ($2\theta = 44^\circ$), inferring that CCB was an amorphous carbon and that some of it was graphitized after pretreatment [29]. However, the CCB peak weakened after Fe₃O₄ loading, possibly because the diffraction peak of the metal oxide crystal masked the diffraction peak of the amorphous state [30]. The main diffraction peaks of Fe₃O₄/CCB well matched the standard card of Fe₃O₄ (JCPDS No. 99–0073). The results showed that the spinel structure of Fe₃O₄ was retained in the composite catalyst. Concretely, diffraction peak of Fe₃O₄/CCB ($2\theta = 30.25^\circ, 35.57^\circ, 43.14^\circ, 53.40^\circ, 57.05^\circ$ and 62.83°) could be observed, consistent with (2 2 0), (3 1 1), (4 0 0), (4 2 2), (5 1 1) and (4 4 0) crystal planes, respectively. The results showed that magnetic catalysts were successfully prepared.

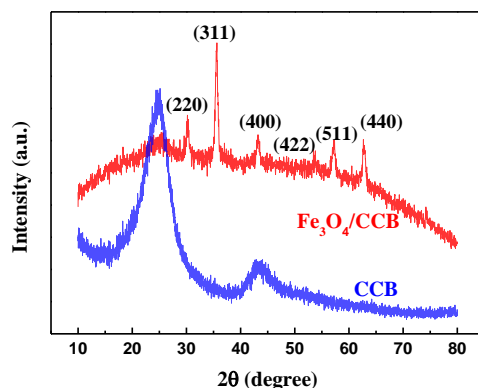


Figure 3. XRD patterns of CCB and Fe₃O₄/CCB particle electrodes.

The magnetic properties of the Fe_3O_4 and $\text{Fe}_3\text{O}_4/\text{CCB}$ particle electrodes were evaluated by VSM analysis (Figure 4). The results displayed that the saturation magnetization (M_s) of $\text{Fe}_3\text{O}_4/\text{CCB}$ (24.8 emu/g) was distinctly lower than that of Fe_3O_4 (49.7 emu/g), which was probably because the load on the CCB weakened a part of the magnetic strength. Although the magnetic saturation is reduced, the $\text{Fe}_3\text{O}_4/\text{CCB}$ catalysts can still be simply separated from the electrocatalytic system by a magnet.

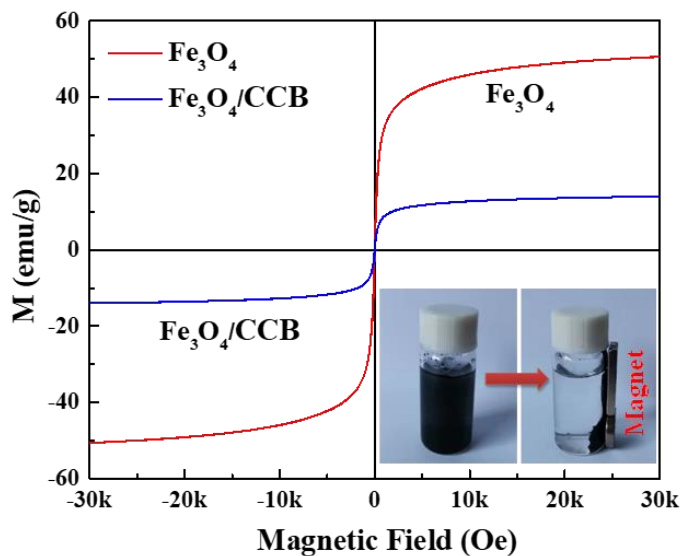


Figure 4. VSM analysis of Fe_3O_4 and $\text{Fe}_3\text{O}_4/\text{CCB}$ particle electrodes.

To investigate the catalytic performance of $\text{Fe}_3\text{O}_4/\text{CCB}$, LSV tests were conducted. The nanoparticle catalyst was deposited onto a GCE as the working electrode, a Pt electrode was used as the counter electrode, and the reference electrode was an SCE. As shown in Figure 5(a), $\text{Fe}_3\text{O}_4/\text{CCB}$ presented a faster reaction rate than CCB and pure Fe_3O_4 , illustrating that the combination of CCB and Fe_3O_4 could increase the contact interface area between the electrode and the electrolyte, which promoted the electron transfer efficiency. The oxygen evolution potential (OEP) is the intersection of the tangent and the horizontal axis, which determines the hydroxyl radical generation capacity and current efficiency [31]. As clearly seen, $\text{Fe}_3\text{O}_4/\text{CCB}$ could stimulate the electrochemical reaction at a low potential, and the current increased rapidly, indicating that extensive $\cdot\text{OH}$ radicals were released in the reaction system, which speeded up the electrocatalytic reaction. $\text{Fe}_3\text{O}_4/\text{CCB}$ has higher catalytic activity and electrical conductivity, which can accelerate the electron transfer between the electrode and the solution interface.

The Nyquist plots (Figure 5b) of the $\text{Fe}_3\text{O}_4/\text{CCB}$ nanoparticle electrodes were obtained by EIS. The resistance (R_s) of the electrolyte solution is the real axis intercept at high frequency, and the charge transfer resistance (R_{ct}) is the semicircle diameter in the high frequency range [32]. The R_{ct} of $\text{Fe}_3\text{O}_4/\text{CCB}$ was obviously the smallest, as shown in Figure 5, which might be attributed to the addition of Fe_3O_4 increasing the CCB active sites and the direct interface contact area, thereby reducing the R_{ct} of $\text{Fe}_3\text{O}_4/\text{CCB}$. This demonstrated that the composites of the metal oxide and CCB could effectively

improve the electronic conductivity and electrocatalytic reaction rate, so that organic pollutants could be sufficiently degraded in a short time and the degradation efficiency enhanced [33].

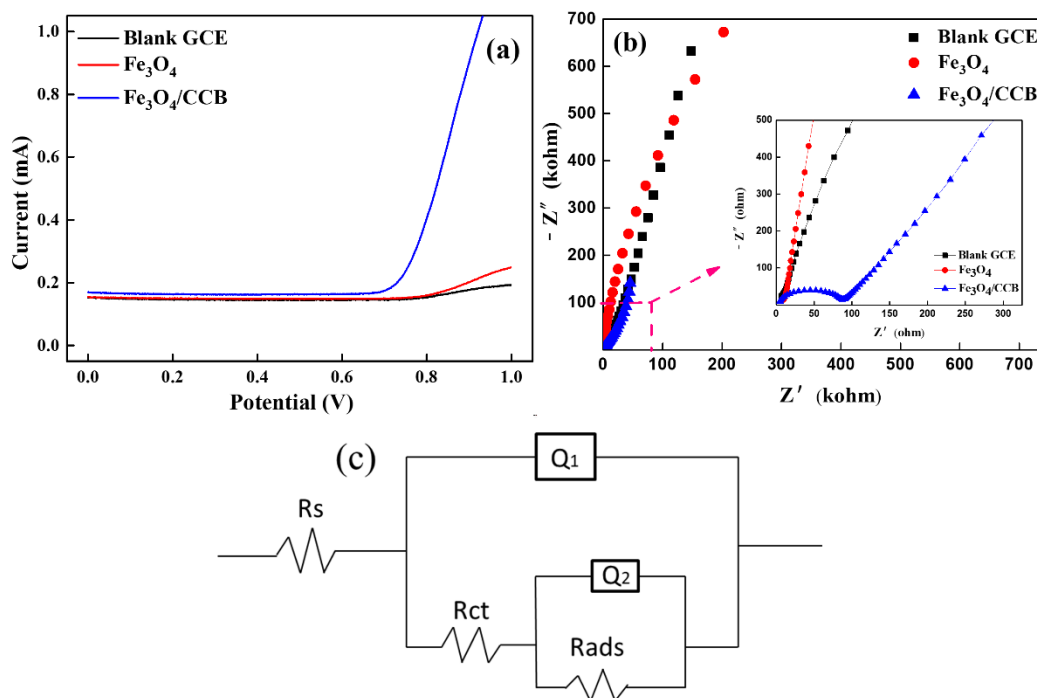


Figure 5. Electrochemical properties of Fe₃O₄/CCB: (a) LSV curves of blank GCE, pure Fe₃O₄ and Fe₃O₄/CCB particle electrodes; (b) Nyquist plots of the different electrodes, where the inset shows a magnified Nyquist image of the high frequency region; (c) equivalent circuit model.

3.2 Effects of different factors on MO degradation

The reaction conditions have a significant influence on the electrocatalytic degradation effect. Therefore, factors including applied voltage, electrolyte concentration, pH, amount of catalyst, initial MO concentration and current density were examined, and the results are displayed in Figure S.

Applied voltage: Increasing the voltage can accelerate electron transfer, which accelerates the electrocatalytic reaction rate, implying a higher pollutant degradation rate. When the applied voltage was increased from 3 V to 5 V, a marked improvement in the COD degradation rate was observed (Figure S1(a)). Further increasing the voltage to 8 V and 10 V led to little improvement in the degradation effect. Similarly, in the first 30 minutes of the reaction, the MO decolorization rate increased following the voltage increased; as the electrolysis reaction proceeded, the highest decolorization rate was observed at 5V (Figure S1(b)). The reason might be that an appropriate increase in the voltage was beneficial to polarization of the catalyst particles; Besides, the electrochemical process would be promoted with more ·OH radical production. However, excessive electrolytic voltage would aggravate the side reactions of oxygen absorption and hydrogen evolution [34], which would not be conducive to the removal of MO and increases the cost. The optimal applied voltage of 5 V was set.

Electrolyte concentration: The conductivity of the wastewater solution requires an external

electrolyte. In Figure S2, the effect of increasing the electrolyte concentration of Na_2SO_4 from 0.04 mol/L to 0.06 mol/L on the degradation of MO was studied. We found that 0.05 mol/L was the optimal degradation condition, and the COD removal rate and decolorization rate were 75.93% and 87.12%, respectively. This might have occurred because a proper concentration of the electrolyte could enhance the conductivity of MO solution, boosting the electrocatalytic process. However, excessive Na_2SO_4 might affect the production of $\cdot\text{OH}$ radicals. When the electrolyte concentration was too high, excess negative ions (SO_4^{2-}) adsorbed on the anode surface under the electric field, resulting in a decrease in active sites, which hindered the electrochemical reaction [34]. As a result, the electrochemical performance of the whole system was weakened [35,36]. Given these experimental data, 0.05 mol/L was selected as the optimal electrolyte concentration for MO electrocatalytic degradation.

Initial pH: The solution pH is important in electrocatalytic degradation processes. Moreover, the pH not only impacts the quantity of active substances and the surface charge state of the catalyst, but also affects the breakage of the organic structure in the degradation process [37]. Hence, a wider range of pH values from 3 to 11 was researched, as shown in Figure S3. The pollutants were rapidly degraded within the first 30 minutes, and then the degradation rate gradually slowed down. This might have occurred because the early reactants were sufficient and the rapid formation of $\cdot\text{OH}$ radicals accelerated the reaction; as the reaction proceeded, the rate of $\cdot\text{OH}$ radical generation gradually decreased with the consumption of Fe^{2+} [38]. When the solution was alkaline, the COD degradation effect worsened. From the results, the lower the pH is, the better the COD degradation. When the pH was 3-9, the MO decolorization rate difference in the first 15 minutes was not obvious, but the decolorization rate was the worst at pH=11 (Figure S3(b)). Hydrogen peroxide easily decomposes under alkaline conditions, hindering the formation of $\cdot\text{OH}$ radicals [39]. After 90 minutes, the highest COD removal rate and MO decolorization rate were 75.02% and 93.75%, respectively, at pH=5. Under this condition, the number of $\cdot\text{OH}$ groups increased to boost the formation of reactive oxygen species (ROS), which was beneficial to the enhanced catalytic activity [40]. Therefore, 5 was the optimal pH.

Catalyst dosage: The effect on the COD removal rate and decolorization rate of MO solution was investigated when the dosage of the particulate catalyst was increased from 1.0 g/L to 2.4 g/L. The results are shown in Figure S4. The addition of an appropriate amount of catalyst particles increased Fe^{2+} and Fe^{3+} , and the accelerated decomposition of H_2O_2 increased $\cdot\text{OH}$ radical production, thus improving the removal performance [41]. Furthermore, the excessive presence of the catalyst in the reaction system caused $\cdot\text{OH}$ to react with Fe^{2+} , and consumed the active material [42,43]. Consequently, 2.0 g/L of the $\text{Fe}_3\text{O}_4/\text{CCB}$ particle electrodes was chosen as being optimal for further investigations.

Initial MO concentration: As shown in Figure S5, the COD removal rate and decolorization rate were affected by different initial concentrations of MO. When the initial concentration of MO was 50 mg/L and 400 mg/L, the low concentration of MO was almost completely decolorized after 30 minutes of the electrocatalytic reaction, and the COD degradation rates were 81.7% and 58.5%, respectively. Additionally, the MO degradation efficiencies of MO per unit electrode plate area were 5.04% and 8.67%, respectively. According to the calculation results that the degradation efficiency for high-concentration wastewater exceeded that for low-concentration wastewater. Because the total amount of pollutants in high-concentration wastewater was large, it took longer to degrade.

Current density: The current density is a major factor in the pollutant removal efficiency, and an

important indicator for measuring energy consumption. Therefore, the removal effect of the current density (from 6 mA/cm² to 20 mA/cm²) on the MO molecules was investigated. In Figure S6, the reaction degradation rate reached the fastest in 0-30 min, and then the degradation efficiency gradually slowed down. During the initial period of the electrolytic reaction, MO molecules easily contacted anode plate and Fe₃O₄/CCB particle electrodes, and were oxidized and degraded directly or indirectly, thus accelerating the degradation rate. However, as the reaction progressed, some intermediates still occupied the active sites, resulting in fewer active species that could contact MO molecules, and thus a lower degradation rate. When the current density was 15 mA/cm², the COD removal rate and decolorization rate reached maximum values of 73.76% and 92.31%; while the current density continued to increase to 20 mA/cm², the removal effect decreased. This showed that an appropriate increase in the current density would promote the electrochemical reaction, while a too large current density would not only increase energy consumption, but also might lead to side reactions [44]. 15 mA/cm² was the optimal current density for this experiment.

The optimal applied voltage, Na₂SO₄ electrolyte concentration, initial solution pH, catalyst dosage, initial MO concentration and current density in this work were 5 V, 0.05 mol/L, 5, 2.0 g/L, 400 mg/L, and 15 mA/cm², respectively.

In addition, first-order reaction kinetics and second-order reaction kinetics were used to simulate the kinetic characteristics of the electrochemical degradation of MO. The results in Figure 6(a, b) show that the COD removal rate conforms to the pseudo-second-order kinetic reaction model (formula 1), and the decolorization rate of MO conforms to the pseudo-first-order kinetic reaction model (formula 2). According to the fitting results of the COD removal rate in the MO solution, the catalytic activity of Fe₃O₄/CCB (0.0593 min⁻¹) visibly outperforms that of the two-dimensional system without the catalyst (0.0182 min⁻¹) and the Fe₃O₄ system (0.0193 min⁻¹). Similarly, the decolorization efficiency when adding the Fe₃O₄/CCB catalyst (0.0250 min⁻¹) is significantly higher than that in the two-dimensional reaction (0.0147 min⁻¹) and Fe₃O₄ (0.0187 min⁻¹) system. This proves that the presence of Fe₃O₄ boosts the catalytic reaction. The catalytic activity of Fe₃O₄ is low, even though its Fe content is much greater than that of the composite catalyst, which is probably because of the small specific surface area caused by agglomeration. Loading of Fe₃O₄ on CCB reduces agglomeration and increases the specific surface area [45]. Based on these results, it can be said that there is a synergistic effect between Fe₃O₄ and CCB, thereby improving the catalytic performance.

$$\frac{1}{C_t} - \frac{1}{C_0} = kt \quad (1)$$

$$-\ln \frac{A_t}{A_0} = k't + b \quad (2)$$

Where t (min) is the electrochemical degradation time of MO; C₀ and C_t (mg/L) represent the COD concentrations in MO solution at the beginning and time t, respectively; A₀ and A_t represent the absorbances of MO solution at the beginning and time t, respectively; k and k' (min⁻¹) are the reaction rate constants.

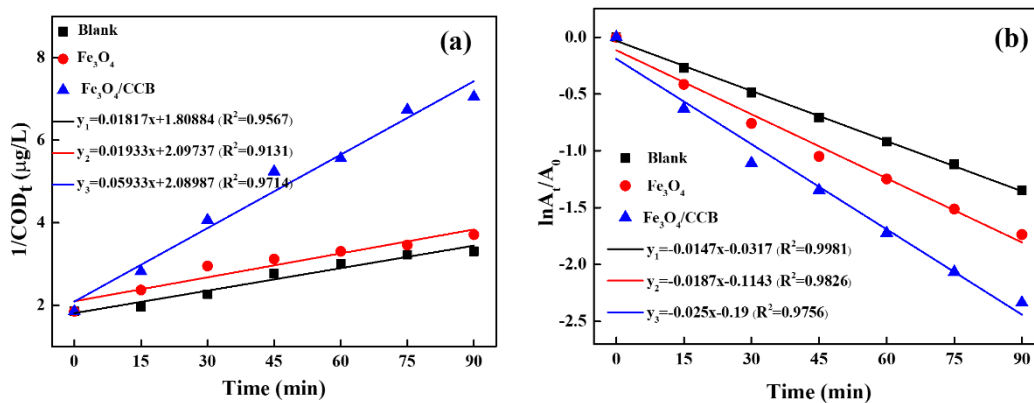


Figure 6. Dynamic fitting (a) COD removal rate; (b) decolorization rate of MO (the optimal conditions were $U=5$ V, $\text{Na}_2\text{SO}_4=0.05$ mol/L, $\text{pH}= 5$, dosage= 2.0 g/L, $\text{MO}=400$ mg/L).

3.3 Reusability and stability of $\text{Fe}_3\text{O}_4/\text{CCB}$ particle electrodes

The reusability and stability of the $\text{Fe}_3\text{O}_4/\text{CCB}$ particle electrodes represent their industrial application value. The optimal degradation conditions of MO were $U = 5$ V, $\text{pH} = 5$, $\text{Na}_2\text{SO}_4 = 0.05$ mol/L, and $\text{Fe}_3\text{O}_4/\text{CCB} = 2.0$ g/L.

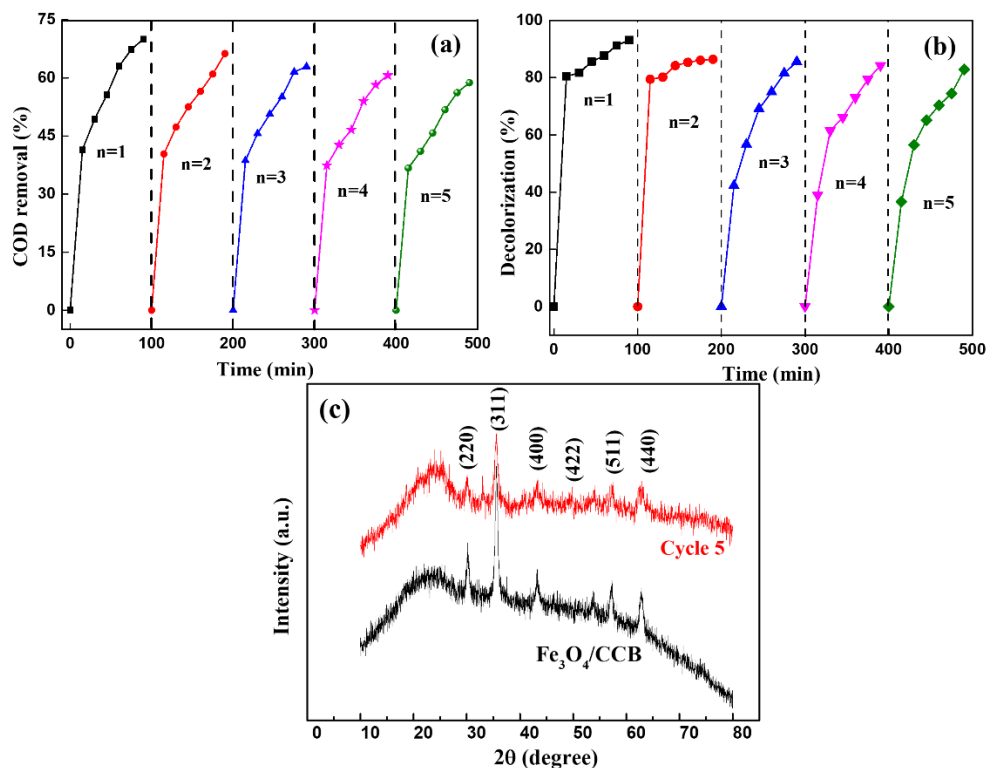


Figure 7. (a) COD concentration changes; (b) MO decolorization rate change over 5 times catalyst cycles; (c) XRD patterns of CCB and $\text{Fe}_3\text{O}_4/\text{CCB}$ particle electrodes over 5 cycles.

After each use, the separated catalyst was washed with ethanol and deionized water many times

and dried. Then the above operation was repeated for the subsequent electrolysis experiments. The $\text{Fe}_3\text{O}_4/\text{CCB}$ catalysts were recycled 5 times, and the COD removal rates of the MO wastewater were 70.02%, 66.28%, 62.93%, 60.67%, and 58.76% (Figure 7(a)). The graph of the decolorization rate shows that a high decolorization rate can be reached in the first 15 minutes. After several cycles, the initial decolorization efficiency became lower, but the removal rate still reached 83.83% after 90 minutes (Figure 7(b)). The reason for the decrease in the catalytic performance after the cycling experiment may be that part of the catalyst was lost during recovery.

Thus, the number of times the particle electrodes can be reused is limited because the small particles will be lost when repeated washing occurs [46]. Meanwhile, when the electrode material is under high pressure for a long time, the strong oxidizing atmosphere and the formation of surface bubbles will cause irreversible damage to the electrode plate and the catalyst, and they will lose their activity [47]. In Figure 7(c), after five cycles, the XRD peak position of the particles remained almost unchanged. The full width at half maximum (FWHM) of the particles before use was 0.758° , whereas that after five cycles was 0.547° . The FWHM of the catalyst particles decreased. According to the Scherrer equation, the particle size of the catalyst particles increased after five recycling-reuse cycles and the specific surface area decreased, resulting in a decrease in catalytic active sites, which is also the reason for the decrease in the catalytic efficiency.

3.4. Mechanism analysis

3.4.1 Three-dimensional fluorescence spectrum analysis

Three-dimensional fluorescence spectra were used to study the changes in organic compounds before and after the catalytic treatment of MO wastewater by the synthesized catalyst. In Figure 8(a), the fluorescence intensity of MO was weak before electrochemical treatment, the main characteristic peaks located at $\text{Em}/\text{Ex}=355/230$ nm, which may be because the azo bond has a defluorescence effect [48]. In Figure 8(b,c), the fluorescence intensity of MO gradually decreased with the oxidation process of the $\text{Fe}_3\text{O}_4/\text{CCB}$ nanoparticle electrodes. At the same time, a redshift occurred in the peaks position, indicating that the azo bond of MO was broken and that an aromatic small molecule with a benzene ring was produced in the degradation process. Hence, the synthesized $\text{Fe}_3\text{O}_4/\text{CCB}$ particle electrodes can degrade MO wastewater in this 3D electrochemical system and achieve the purpose of this experiment.

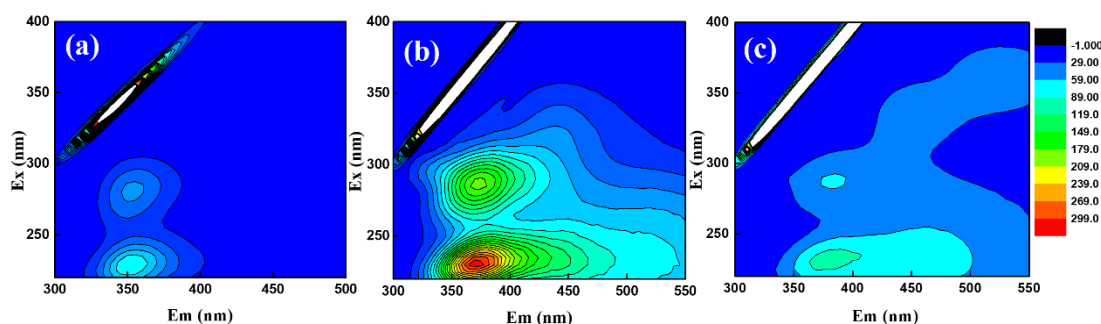


Figure 8. Three-dimensional fluorescence spectra to characterize the degradation process of MO: (a) before degradation; (b) after 15 minutes degradation by $\text{Fe}_3\text{O}_4/\text{CCB}$ particle electrodes; (c) after 90 minutes degradation by $\text{Fe}_3\text{O}_4/\text{CCB}$ particle electrodes.

3.4.2 UV-vis absorption spectra analysis

The variation in the UV-vis spectra of the MO solution during the electrochemical degradation process using the $\text{Fe}_3\text{O}_4/\text{CCB}$ particle electrodes is shown in Figure 9. Before electrochemical degradation, a strong absorption peaks appeared at 464 nm, which was designated as the absorbance of chromogenic azo groups in MO [49]. Along with the electrochemical oxidation reaction proceeded, the absorbance of the MO solution dramatically decreased, and the absorbance was close to completely disappearing after 90 min, indicating that the chromogenic group of the MO was eliminated. As the electrochemical reaction progressed, the MO absorption peak gradually weakened, which was a common phenomenon in other MO removal methods [50]. The reason was that the hydroxyl radicals generated by electrolysis in the 3D electrocatalytic system first destroyed the azo bonds in the MO structure, and then gradually decomposed into small molecules. Eventually, the small molecules degraded into CO_2 and H_2O [51].

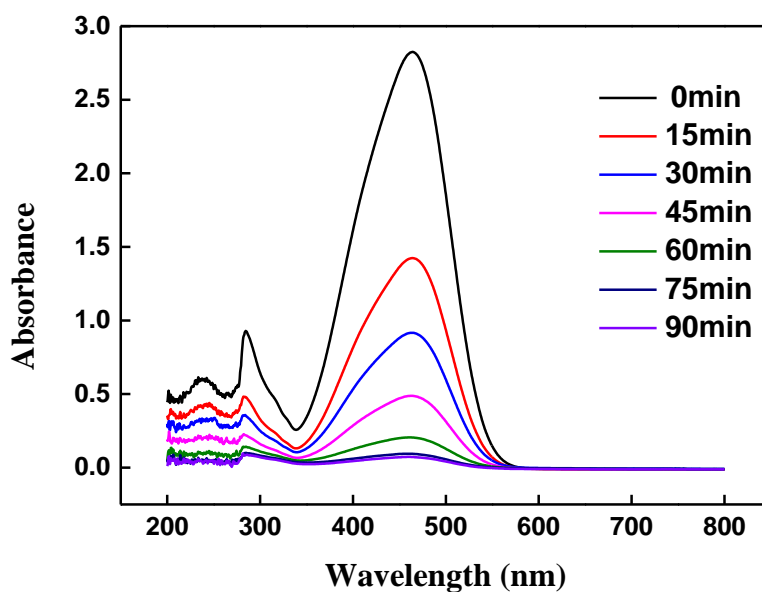


Figure 9. UV-vis spectra of MO during the electrochemical oxidation process by $\text{Fe}_3\text{O}_4/\text{CCB}$ particle electrodes.

3.4.3 Trapping experiments of radicals

Then, 10mM TBA was added to the electrolysis system as a quencher of $\cdot\text{OH}$ radicals. In Figure 10, the decolorization rate and COD removal rate of MO solutions attained 93.3% and 75.02%, respectively, without free radical quenching agents. After adding TBA, the decolorization rate and COD removal rate of MO solutions dropped to 73.8% and 30.2%, respectively, and it could be deduced that $\cdot\text{OH}$ played a significant role in MO degradation. By all accounts, the experimental results displayed that $\cdot\text{OH}$ was the key to the electrocatalytic degradation in this system.

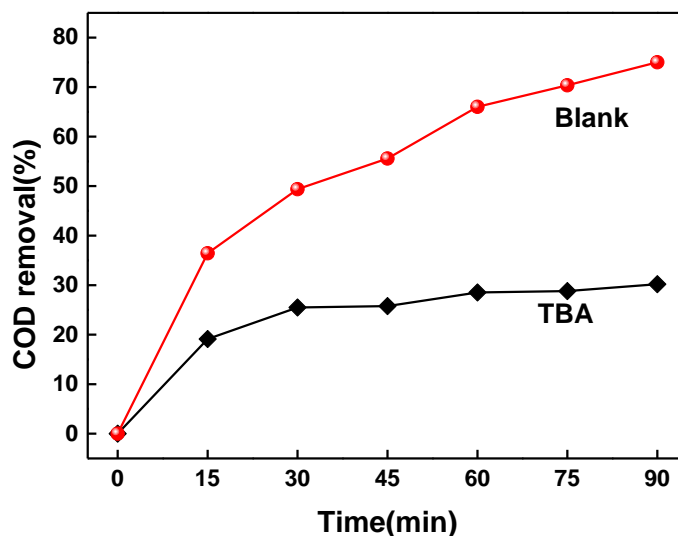


Figure 10. Effect of adding a free radical scavenger on MO degradation.

3.4.4 Electrocatalytic mechanism

H_2O_2 and $\cdot\text{OH}$ radicals are regarded as the main ROSs in the 3D electrode catalytic degradation reactions [52]. To clarify the mechanism of the enhanced electrocatalytic activity, the variations of H_2O_2 and $\cdot\text{OH}$ radical contents in the reaction were detected.

Fig. 11 shows the cumulative concentration of H_2O_2 at different electrolysis times. The cumulative concentration of H_2O_2 reached the highest value in the first 30 min reaction, then gradually decreased and stabilized. In the early reaction stage, dissolved oxygen was easily adsorbed on the active sites on the cathode surface, and quickly reacted with electrons to generate H_2O_2 [53]. However, Fe^{2+} in the catalyst reacted with H_2O_2 to produce $\cdot\text{OH}$ radicals with the prolongation of electrolysis time. When the combination rate of H_2O_2 and Fe^{2+} and its generation rate reached a balance, the H_2O_2 concentration inclined to be stable.

The cumulative concentration of $\cdot\text{OH}$ generated in the system increased with the reaction time and then gradually stabilized in Fig. 11. The produced $\cdot\text{OH}$ radicals were mainly attributed to two aspects. On the one hand, the anode directly produced $\cdot\text{OH}$ radicals by electrolysis; on the other hand, Fe^{2+} could react with H_2O_2 to form $\cdot\text{OH}$ radicals. The $\cdot\text{OH}$ concentration also basically inclined to be stable with extension of the time, which was probably because the pollutant molecules and intermediate products consumed $\cdot\text{OH}$ radicals. It could be seen from the figure 11 that H_2O_2 and $\cdot\text{OH}$ could be continuously produced throughout the reaction process, which was why the system could efficiently degrade MO wastewater.

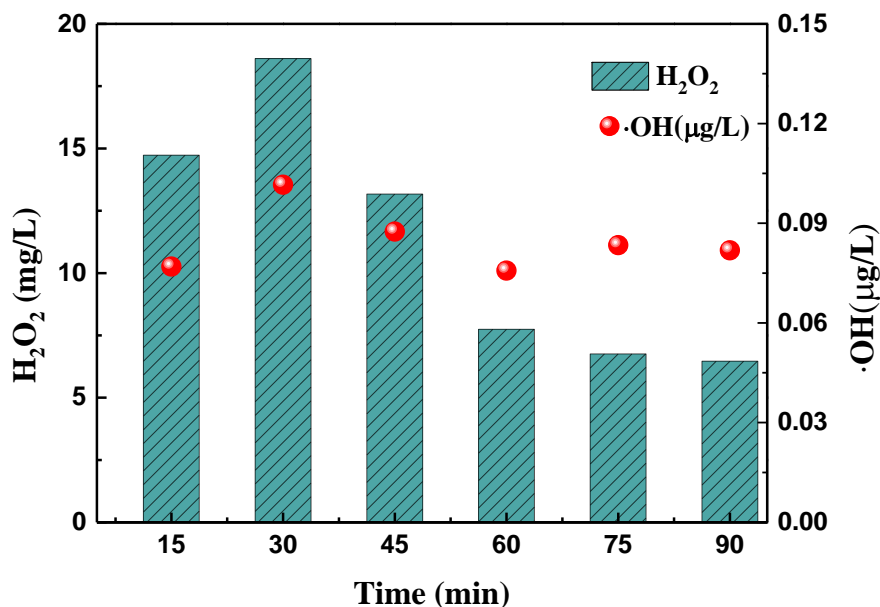
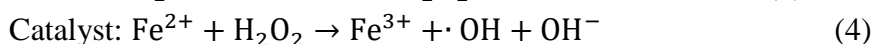
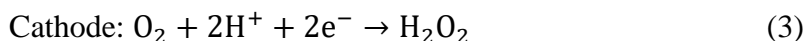
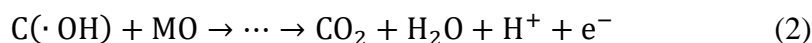
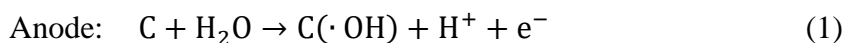


Figure 11. Content of active groups in the Fe₃O₄/CCB system.

A possible electro-oxidative MO degradation pathway is shown in Figure 12. CCB has excellent electrical conductivity, and its chain structure forms more conductive paths [54]. The surface of the CCB after pretreatment was rough, which is beneficial to the loading of Fe₃O₄. Therefore, the electrochemical performance of Fe₃O₄ supported CCB was good. MO molecules were directly oxidized at the anode. The oxygen dissolved in water was adsorbed on the surface of the Fe₃O₄/CCB particle electrodes and cathode plate, thus obtaining electrons and undergoing a reduction reaction to generate H₂O₂. The Fe²⁺ decomposed by the catalyst underwent the Fenton reaction with H₂O₂ to produce strong oxidizing hydroxyl radicals, and then ·OH radicals oxidized MO. The 3D electrochemical system had both a direct oxidation process and an indirect oxidation process. The double oxidation firstly led to the breaking of the azo bond to produce an intermediate product with a benzene ring, which was then continuously degraded and mineralized through the reaction, finally generated CO₂ and H₂O [55].

The main reaction process was as follows equation.



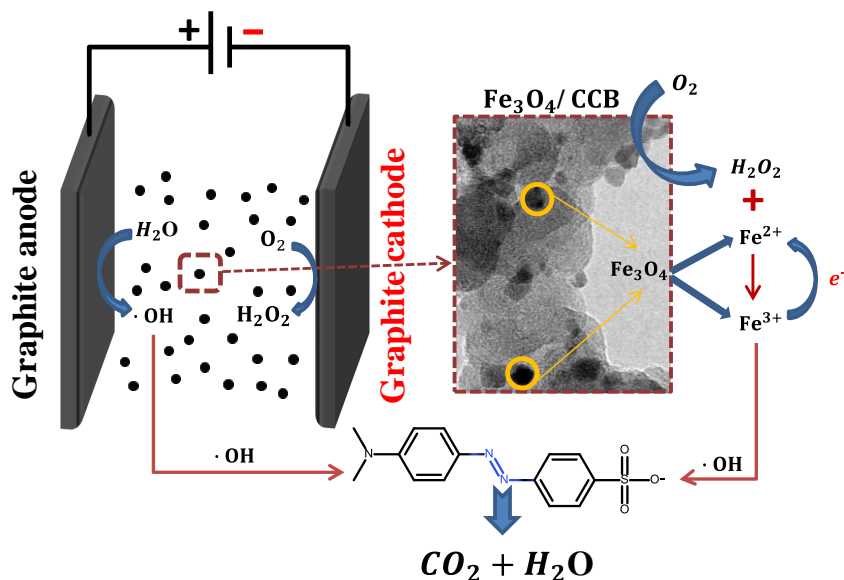


Figure 12. Reaction mechanism of the $\text{Fe}_3\text{O}_4/\text{CCB}$ system.

4. CONCLUSIONS

Pure Fe_3O_4 and $\text{Fe}_3\text{O}_4/\text{CCB}$ particle electrodes were synthesized by a simple impregnation method. TEM and XRD results showed that the structure of CCB was conducive to uniform dispersion of Fe_3O_4 . The average size of the prepared nanoparticles was 12.2 nm. $\text{Fe}_3\text{O}_4/\text{CCB}$ could be easily recycled due to magnetism. The optimal conditions were 5 V applied voltage, 0.05 mol/L concentration of electrolyte, pH 5, the dosage of $\text{Fe}_3\text{O}_4/\text{CCB}$ was 2.0 g/L and 15 mA/cm^2 current density. After 90 minutes of electrolysis, the COD removal rate was 75.02%, and the decolorization rate of MO reached 93.75%. The catalytic activity of $\text{Fe}_3\text{O}_4/\text{CCB}$ remained at 83.83% after 5 reuse cycles, indicating the good stability of the catalysts. Moreover, the fitting calculation verified that the COD removal rate followed pseudo-second-order kinetics and that the decolorization rate accorded with pseudo-first-order kinetics. Finally, the degradation mechanism of MO by $\text{Fe}_3\text{O}_4/\text{CCB}$ was discussed, which was mainly because the structure of CCB promoted electron transfer, which facilitated the formation of H_2O_2 and the $\text{Fe}^{3+}/\text{Fe}^{2+}$ cycle, thus increasing the content of $\cdot\text{OH}$. This promotes the application prospects in the dye removal process.

ACKNOWLEDGEMENTS

This work is financially supported by Science and Technology Commission of Shanghai (19DZ2271100) and Natural Science Foundation of Shanghai (Grant Nos. 20ZR1421500).

DECLARATION OF INTEREST

The authors do not have conflicts of interest in the publication of this manuscript.

SUPPORTING MATERIALS:

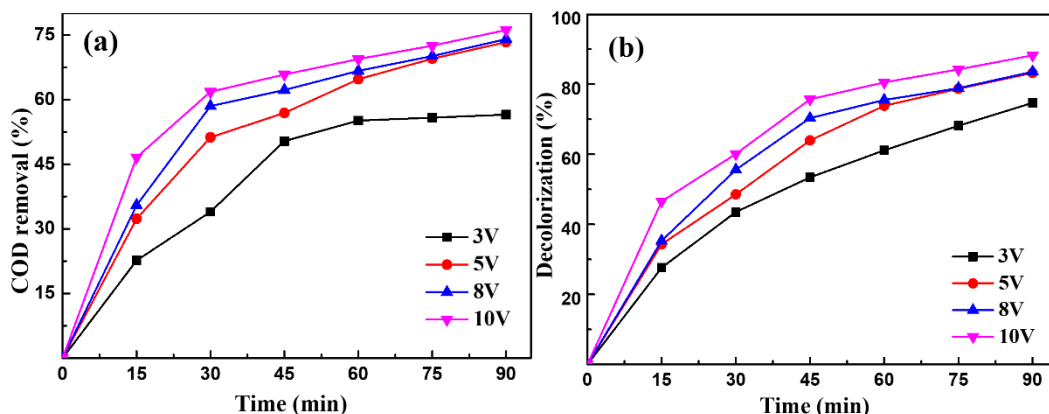


Figure. S1 Effect of applied voltage on the COD removal and decolorization rate during electrolysis of the MO. Initial MO concentration: 400 mg/L, Na₂SO₄: 0.05 mol/L, catalyst dosage: 2.0 g/L, pH: without adjustment.

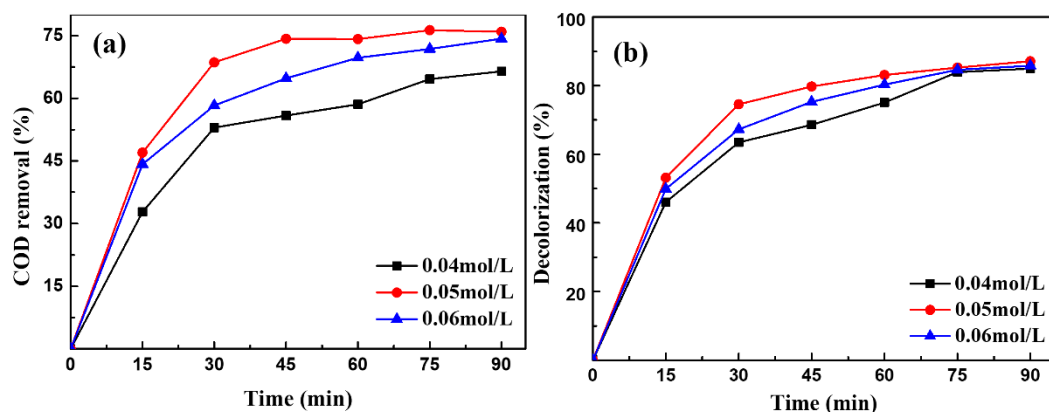


Figure. S2 Effect of Na₂SO₄ concentration on the COD removal and decolorization rate during electrolysis of the MO. Applied voltage: 5 V, initial MO concentration: 400 mg/L, catalyst dosage: 2.0 g/L, pH: without adjustment.

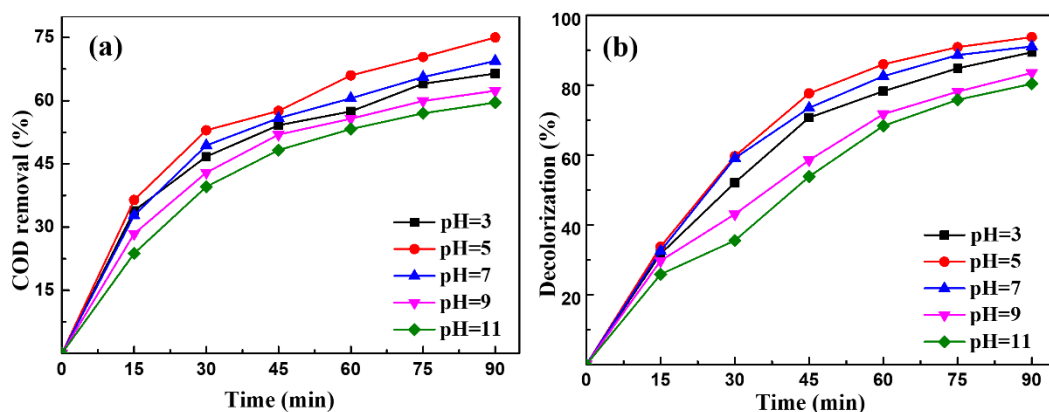


Figure. S3 Effect of initial pH on the COD removal and decolorization rate during electrolysis of the MO. Applied voltage: 5 V, initial MO concentration: 400 mg/L, Na₂SO₄: 0.05 mol/L, catalyst dosage: 2.0 g/L.

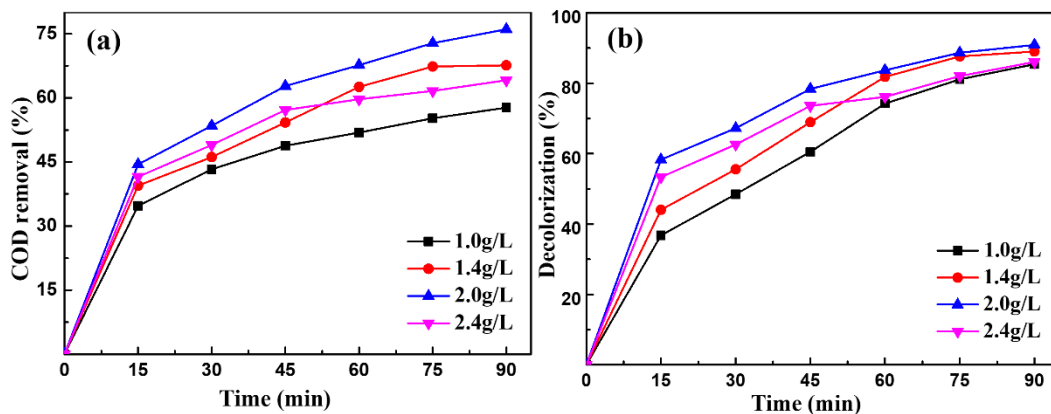


Figure. S4 Effect of catalyst dosage on the COD removal and decolorization rate during electrolysis of the MO. Applied voltage: 5 V, initial MO concentration: 400 mg/L, Na₂SO₄: 0.05 mol/L, initial pH: 5.

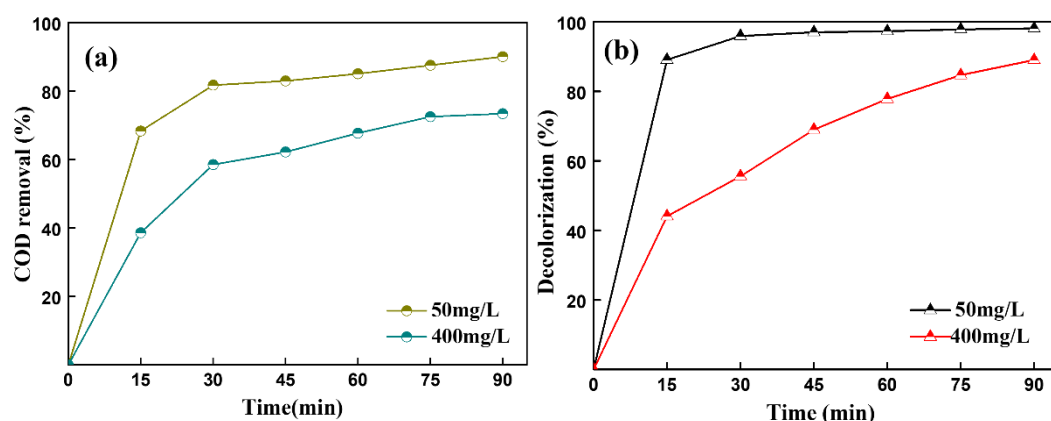


Figure. S5 Effect of initial MO concentration on the COD removal and decolorization rate during electrolysis of the MO. Applied voltage: 5 V, Na₂SO₄: 0.05 mol/L, initial pH: 5, catalyst dosage: 2.0 g/L.

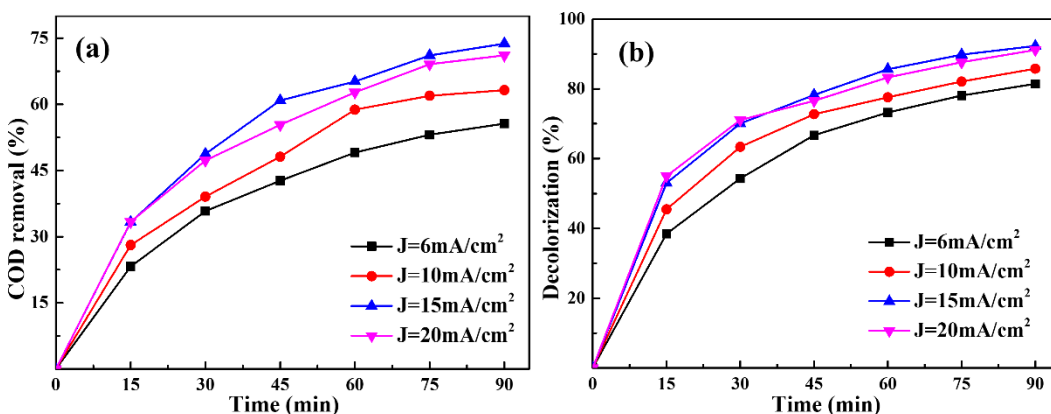


Figure. S6 Effect of current density on the COD removal and decolorization rate during electrolysis of the MO. Initial MO concentration: 400 mg/L, applied voltage: 5 V, Na₂SO₄: 0.05 mol/L, initial pH: 5, catalyst dosage: 2.0 g/L.

Fig S1-S6 | COD removal rate of MO under different conditions: (a) applied voltage, (b) electrolyte concentration, (c) initial pH, (d) particle electrodes dosage, (e) initial concentration of MO,

(f) current density (The best operation condition was $U = 5$ V, $\text{Na}_2\text{SO}_4 = 0.05$ mol/L, $\text{pH} = 5$, dosage = 2.0 g/L, $\text{MO} = 400$ mg/L, and $J = 15$ mA/cm²).

References

1. K. Paździor, L. Bilińska and S. Ledakowicz, *Chem. Eng. J.*, 376 (2019) 12597.
2. Y. Zhang, F. Gao, B. Wanjala, Z. Y. Li, G. Cernigliaro and Z. Y. Gu, *Appl. Catal. B- Environ.*, 199 (2016) 504-513.
3. Y. Gao, S. Q. Deng, X. Jin, S. L. Cai, S. R. Zheng and W.G. Zhang, *Chem. Eng. J.*, 357 (2019) 129-139.
4. T. T. Wei, L. Wu, F. Yu, Y. Lv, L. Chen, Y.L. Shi and B. Dai, *RSC Adv.*, 8 (2018) 39334.
5. H. M. Xu, X. F. Sun, S. Y. Wang, C. Song and S.G. Wang, *Sep. Purif. Technol.*, 204 (2018) 205-260.
6. F. F. Dias, A. A. S. Oliveira, A. P. Arcanjo and F. C. C. Moura, *Appl. Catal. B- Environ.*, 186 (2016) 136-142.
7. K. E. Hassani, D. Kalnina, M. Turks, B. H. Beakou and A. Anouar, *Sep. Purif. Technol.*, 210 (2019) 764-774.
8. Q. M. Chen, X. D. Zhang, S. Q. Li, J. K. Tan, C. J. Xu and Y. M. Huang, *Chem. Eng. J.*, 395 (2020) 125130.
9. A. Ansari and D. Nematollahi, *Appl. Catal. B- Environ.*, 261 (2020) 118226.
10. A. Özcan, A. A. Özcan, Y. Demirci and E. Sener, *Appl. Catal. B- Environ.*, 200 (2017) 361-371.
11. S. Payra, S. Challagulla, Y. Bobde, B. Chakraborty and B. Ghosh, *J. Hazard. Mater.*, 373 (2019) 377-388.
12. R. Yamaguchi, S. Kurosu, M. Suzuki and Y. Kawase, *Chem. Eng. J.*, 334 (2018) 1537-1549.
13. L. Bilinska, M. Gmurek and S. Ledakowicz, *Process Saf. Environ.*, 109 (2017) 420-428.
14. S. Liu, Z. Y. Wang, J. F. Li, C. Zhao, X. L. He and G. Yang, *Chemosphere*, 213 (2018) 377-383.
15. K. He, G. Q. Chen, G. G. Zeng, A. W. Chen, Z. Z. Huang, J. B. Shi, T. T. Huang, M. Peng and L. Hu, *Appl. Catal. B- Environ.*, 228 (2018) 19-28.
16. A. Rahmani, M. Salari, K. Tari, N. Shabanloo and S. Bajalan, *Chem. Eng. J.*, 8 (2020) 104468.
17. L. Gui, Z. Chen, B. Y. Chen, Y. Z. Song, Q. Yu, W. Zhu, Q. Hu, Y. Y. Liu, Z. Y. Zheng, Z. Lv, H. J. You and F. Yeasmin, *J. Hazard. Mater.*, 399 (2020) 123018.
18. J. Li, J. F. Yan, G. Yao, Y. H. Zhang, X. Li and B. Lai, *Chem. Eng. J.*, 361 (2019) 1317-1332.
19. Z. Y. Wang, B. Song, J. F. Li and X. L. Teng, *Chemosphere*, 17 (2020) 128652.
20. A. Šuligoj, A. Ristić, G. Dražić, A. Pintar, N. Z. Logar and N. N. Tušar, *Catal. Today*, 358 (2020) 270-277.
21. J. T. Tang and J. L. Wang, *Chem. Eng. J.*, 351 (2018) 1085-1094.
22. Q. R. Shi, S. Hwang, H. P. Yang, F. Ismail, D. Su, D. Higgins and G. Wu, *Mater. Today*, 37 (2020) 93-111.
23. K. Konda, S. B. Moodakare, P. L. Kumar, M. Battabyal, J. R. Seth, V.A. Juvekar and R. Gopalan, *J. Power Sources*, 480 (2018) 228837.
24. Y. M. Zhang, Z. Chen, P. P. Wu, Y. X. Duan, L. C. Zhou, Y. X. Lai, F. Wang and S. Li, *J. Hazard. Mater.*, 393 (2020) 120448.
25. H. Ghanbarlou, B. Nasernejad, M. N. Fini, M. E. Simenson and J. Muff, *Chem. Eng. J.*, 395 (2020) 125025.
26. B. L. Hou, B. Z. Ren, R. J. Deng, J. C. Zhu, Z. H. Wang and Z. Li, *RSC Adv.*, 7 (2017) 15455.
27. Y. J. Wang, J. Chen, J. X. Gao, H. S. Meng, S. N. Chai, Y. F. Jian, L. M. Shi, Y. B. Wang and C. He, *Sep. Purif. Technol.*, 272 (2021) 118884.
28. X. Q. Chen, W. Teng, J. W. Fan, Y. Y. Chen, Q. Ma and Y. H. Xue, C. N. Zhang and W. X. Zhang, *J. Hazard. Mater.*, 427 (2022) 127896.

29. Y. Chen, Y. Z. Zhu, M. Tian, C. Chen, X. B. Jia and S. Y. Gao, *Nano Energy*, 59 (2019) 346-353.
30. H. Pourzamani, Y. Hajizadeh and N. Mengelizadeh, *Process Saf. Environ.*, 119 (2018) 271-284.
31. P. Z. Duan, X. Hu, Z. Y. Ji, X. M. Yang and Z. R. Sun, *Chemosphere*, 212 (2018) 594-603.
32. W. L. Yang, Z. J. Deng, Y. J. Wang, L. Ma, K. C. Zhou and L. B. Liu, *Sep. Purif. Technol.*, 293 (2022) 121100.
33. X. L. Guo, J. F. Wan, X. J. Yu and Y. H. Lin, *Chemosphere*, 164 (2016) 421-429.
34. S. X. Chen, J. Li, L. Y. Liu, Q. H. He, L. H. Zhou, T. T. Yang, X. J. Wang, P. He, H. Zhang and B. Jia, *Chemosphere*, 256 (2020) 127139.
35. Y. J. Sun, P. Li, H. L. Zheng, C. Zhao, X. F. Xiao, Y. H. Xu, W. Q. Sun, H. F. Wu and M. J. Ren, *Chem. Eng. J.*, 308 (2017) 1233-1242.
36. Y. W. Yao, C. J. Huang, Y. Yang, M. Y. Li and B. L. Ren, *Chem. Eng. J.*, 350 (2018) 960-970.
37. S. Q. Zhou, L. J. Bu, Z. Shi, C. Bi and Q. H. Yi, *Chem. Eng. J.*, 306 (2016) 719-725.
38. S. Xiao, M. Cheng, H. Zhong, Z. F. Liu, Y. Liu, X. Yang and Q. H. Liang, *Chem. Eng. J.*, 384 (2020) 123265.
39. Y. W. Yao, G. G. Teng, Y. Yang, B. L. Ren and L. L. Gui, *Sep. Purif. Technol.*, 227 (2019) 115684.
40. Y. M. Zhang, D. D. Zhang, L. C. Zhou, Y. L. Zhao, J. Chen, Z. Chen and F. Wang, *Chem. Eng. J.*, 336 (2018) 690-700.
41. D. L. Deng, X. H. Wu, M. Y. Li, S. Qian, B. L. Tang, S. Q. Wei and J. Z. Zhang, *Chemosphere*, 259 (2020) 127488.
42. A. H. Mady, M. L. Baynosa, D. Tuma and J. J. Shim, *Appl. Catal. B- Environ.*, 244 (2019) 946-956.
43. Y. Wang, Y. Y. Xi, H. L. Tian, J. S. Fang, X. C. Quan and Y. S. Pei, *Catal. Today*, 335 (2019) 460-467.
44. D. Y. Feng, Z. J. Shang, P. Xu, H. Y. Yue and X. X. Li, *Electroanal. Chem.*, 906 (2022) 116017.
45. X. L. Teng, J. F. Li, Z. Y. Wang, Z. Wei, C. Z. Chen, K. Q. Du, C. Zhao, G. Yang and Y. Li, *RSC Adv.*, 10 (2020) 24712.
46. F. J. Ren, W. W. Zhu, J. Y. Zhao, H. T. Liu, X. A. Zhang, H. Zhang, H. Zhu, Y. Peng and B. Wang, *Sep. Purif. Technol.*, 241 (2020) 116690.
47. L. J. Chen, Y. Q. Zhang and C. B. Ma, *Chem. Eng. J.*, 393 (2020) 124514.
48. T. T. Zhang, Y. J. Liu, L. Yang, W. P. Li, W. D. Wang and P. Liu, *J. Clean. Prod.*, 258 (2020) 120273.
49. X. J. Liu, Z. M. Chen, W. Q. Du, P. F. Liu, L. Zhang and F. W. Shi, *J. Environ. Manage.*, 311 (2022) 114775.
50. Y. W. Yao, B. L. Ren, Y. Yang, C. J. Huang and M. Y. Li, *J. Hazard. Mater.*, 361 (2019) 141-151.
51. W. Q. Sun, Y. J. Sun, K. J. Shah, H. L. Zheng and B. Ma, *J. Environ. Manage.*, 241 (2019) 22-31.
52. D. Li, T. Y. Sun, L. Wang and N. Wang, *Electrochim. Acta*, 282 (2018) 416-426.
53. Z. Yang, X. B. Gong, L. Peng, D. Yang and Y. Liu, *Chemosphere*, 208 (2018) 665-673.
54. B. Cai, J. F. Feng, Q. Y. Peng, H. F. Zhao, Y. C. Miao and H. Pan, *J. Hazard. Mater.*, 392 (2020) 122279.
55. Y. T. Liu, C. F. Gao, L. F. Liu, T. T. Yu and Y. H. Li, *Sep. Purif. Technol.*, 284 (2022) 120232.